International Journal of Pharmaceutics: X 7 (2024) 100245

Contents lists available at ScienceDirect

International Journal of Pharmaceutics: X

journal homepage: www.sciencedirect.com/journal/international-journal-of-pharmaceutics-x

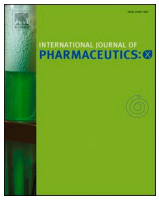

Formulation and evaluation of azithromycin-loaded silver nanoparticles for the treatment of infected wounds

Mohammed S. Saddik [a,*], Mostafa F. Al-Hakkani [b,*], Ahmed M. Abu-Dief [c,d,**], Mohamed S. Mohamed [e], Islam A. Al-Fattah [b], Mahmoud Makki [f], Mohamed A. El-Mokhtar [g,h], Marwa A. Sabet [i], M.S. Amin [c,j], Hoda A. Ahmed [k,l], Khalaf Al-Ghamdi [c], Mostafa K. Mohammad [m], Mohammad H.A. Hassan [n]

[a] Department of Pharmaceutics and Clinical Pharmacy, Faculty of Pharmacy, Sohag University, P.O. Box 82524, Sohag 82524, Egypt
[b] Department of Research, Development, and Stability, UP Pharma, Industrial Zone, Arab El Awamer, Abnoub, 76, Assiut, Egypt
[c] Chemistry Department, College of Science, Taibah University, P.O. Box 344, Al-Madinah Al-Munawwarah, Saudi Arabia
[d] Chemistry Department, Faculty of Science, Sohag University, Sohag 82524, Egypt
[e] Department of Pharmaceutics and Pharmaceutical Technology, Faculty of Pharmacy, Al-Azhar University, Assiut 71524, Egypt
[f] Department of Dermatology and Andrology, Faculty of Medicine [Assiut], Al-Azhar University, Assiut 71524, Egypt
[g] Gilbert and Rose-Marie Chagoury School of Medicine, Lebanese American University, Byblos, Lebanon
[h] Department of Medical Microbiology and Immunology, Faculty of Medicine, Assiut University, Assiut 71515, Egypt
[i] Department of Microbiology and Immunology, Faculty of Pharmacy, Sphinx University, New-Assiut 71684, Egypt
[j] Chemistry Department, Faculty of Science, Ain Shams University, Cairo, Egypt
[k] Chemistry Department, Faculty of Science at Yanbu, Taibah University, Yanbu 46423, Saudi Arabia
[l] Department of Chemistry, Faculty of Science, Cairo University, Cairo 12613, Egypt
[m] Department of Pharmacology and Toxicology, Faculty of Pharmacy, Badr University in Assiut, New Nasser City, West of Assiut, Egypt
[n] Department of Medical Laboratory Technology, Higher Technological Institute for Applied Health Sciences in Minya, Minya, Egypt

ARTICLE INFO

Keywords:
Green biosynthesis
AZM-AgNPs
Adsorption isotherm
Infected wound

ABSTRACT

Infected wounds pose a significant challenge in healthcare, requiring innovative therapeutic strategies. Therefore, there is a critical need for innovative pharmaceutical materials to improve wound healing and combat bacterial growth. This study examined the efficacy of azithromycin-loaded silver nanoparticles (AZM-AgNPs) in treating infected wounds. AgNPs synthesized using a green method with *Quinoa* seed extract were loaded with AZM. Characterization techniques, including X-ray Powder Diffraction (XRD), scanning electron microscope (SEM), transmission electron microscope (TEM), and Uv-Vis analysis were utilized. The agar diffusion assay and determination of the MIC were used to assess the initial antibacterial impact of the formulations on both MRSA and *E. coli*. In addition, the antimicrobial, wound-healing effects and histological changes following treatment with the AZM-AgNPs were assessed using an infected rat model. The nanoparticles had size of 24.9 ± 15.2 nm for AgNPs and 34.7 ± 9.7 nm for AZM-AgNPs. The Langmuir model accurately characterized the adsorption of AZM onto the AgNP surface, indicating a maximum loading capacity of 162.73 mg/g. AZM-AgNPs exhibited superior antibacterial properties in vivo and in vitro compared to controls. Using the agar diffusion technique, AZM-AgNPs showed enhanced zones of inhibition against *E. coli* and MRSA, which was coupled with decreased MIC levels. In addition, in vivo studies showed that AZM-AgNP treated rats had the best outcome characterized by improved healing process, lower bacterial counts and superior epithelialization, compared to the control group. In conclusion, AZM-AgNPs can be synthesized using a green method with Quinoa seed with successful loading of azithromycin onto silver nanoparticles. In vitro and in vivo studies suggest the promising use of AZM-AgNPs as an effective therapeutic agent for infected wounds.

* Corresponding authors.
** Corresponding author at: Chemistry Department, College of Science, Taibah University, P.O. Box 344, Al-Madinah Al-Munawwarah, Saudi Arabia.
E-mail addresses: mohammed.sherif@pharm.sohag.edu.eg (M.S. Saddik), dr.mostafa.farouk.83@gmail.com (M.F. Al-Hakkani), amamohammed@taibahu.edu.sa (A.M. Abu-Dief).

https://doi.org/10.1016/j.ijpx.2024.100245
Received 2 February 2024; Received in revised form 4 April 2024; Accepted 7 April 2024
Available online 9 April 2024

1. Introduction

The skin is the main physical barrier against harmful pathogens. After an injury, the healing process promptly begins to regenerate the injured tissues (Yang et al., 2021). Inadequate repair methods can lead to severe consequences, such as skin loss and the onset of infections. Therefore, it damages underlying tissues and affects the overall systemic function (Sorg et al., 2017). Infection is frequently the main obstacle to healing wounds, especially in cases of chronic wounds. Bacteria are typically present in the natural microbiota of healthy skin and wounds. However, impediments to wound healing may arise due to the presence of a substantial quantity of bacteria, along with the formation of a biofilm (Bowler et al., 2001). Despite advancements in wound management, bacterial and fungal infections remain among the most prevalent and distressing conditions, contributing significantly to both mortality and morbidity (Maheswary et al., 2021). *S. aureus, MRSA, and Pseudomonas aeruginosa* are the dominant microbial pathogens found in individuals with wound infections (Negut et al., 2018). AZM, a second-generation macrolide with broad antibacterial activities, has recently garnered more interest due to its effects on host-defense mechanisms and long-term human conditions (Parnham et al., 2014). Furthermore, it can influence bacterial ribosomes, initiating a series of biochemical reactions. Consequently, this impedes the synthesis of proteins essential for bacterial growth and reproduction, ultimately restraining their proliferation. According to several reports, AZM has demonstrated efficacy against pseudomonas aeruginosa infection. It is noteworthy that, similar to other macrolides, AZM can penetrate bacterial biofilms. The ability to penetrate is widely recognized as the primary mechanism underlying their effectiveness against bacterial biofilms (Imperi et al., 2014).

The green synthesis method is commonly used to produce basic metal nanoparticles due to its cost-effectiveness, non-toxicity, and safety (Hosny et al., 2024; Hosny et al., 2023; Buarki et al., 2022; Onyedikachi et al., 2022; Abu-Dief et al., 2022; Sangili et al., 2021; Sethy et al., 2020; Singh et al., 2018a; Subhapriya and Gomathipriya, 2018).

Compared to other nanomaterials, biofabricated silver nanoparticles have a number of benefits, especially in antibacterial and antibiofilm applications. One of these is their strong antibacterial action against a variety of pathogens, such as viruses, fungi, and bacteria, which is exhibited by their broad-spectrum antimicrobial activity (Krishnamoorthi et al., 2022). They are efficient against a variety of infections due to their broad-spectrum action, which lowers the possibility of resistance developing (Saddik et al., 2021, Abu-Dief et al., 2020). Additionally, it has been demonstrated that silver nanoparticles may successfully prevent and interfere with the formation of biofilms, which poses a serious problem for a number of industries, including healthcare and food processing (Elshazly et al., 2022). Communities of bacteria known as biofilms are imprisoned in an extracellular polymeric matrix that they generate on their own, giving them remarkable resistance to conventional antimicrobial treatments. Furthermore, because biofabricated silver nanoparticles are made by biological processes like microbial or plant extracts, they are typically thought to be less harmful and more biocompatible than chemically generated nanoparticles. As a result, there is less chance of negative consequences on the environment and human health (Some et al., 2019).

Additionally, the biofabrication of silver nanoparticles typically eliminates the need for harsh chemicals and solvents by utilizing renewable and ecologically benign materials like plant extracts or microorganisms (Al-Hakkani, 2020; Al-Hakkani et al., 2021a). As a result, the production process is more environmentally friendly and sustainable. The antimicrobial ingredient may be delivered and released under control using silver nanoparticles in a variety of delivery methods, including hydrogels, nanofibers, and nanocomposites. This may increase the antibacterial effect's potency and longevity. A variety of biomolecules, including polymers, proteins, and antibodies, can be functionalized to improve the selectivity, biocompatibility, and targeted distribution of the biofabricated silver nanoparticles (Singh et al., 2019; Singh et al., 2018b; Some et al., 2019). When compared to certain other nanomaterials or traditional antimicrobial agents, the production process for silver nanoparticles is more cost-effective due to the fact that the most advantageous method of biofabrication frequently employs easily accessible and affordable raw materials. With their antibacterial and antibiofilm qualities, these benefits make biofabricated silver nanoparticles appealing for a variety of uses in healthcare (medical devices, wound dressings), food packaging, water treatment, and environmental remediation (Malaikozhundan et al., 2016; Malaikozhundan et al., 2017).

Nanoparticles produced via green synthesis have various applications, including anti-inflammatory and antimicrobial properties, effective medication transport, biological function, targeting tumors, cancer-fighting properties, and absorption into biological systems (Saddik et al., 2021, Abu-Dief et al., 2020). Additionally, these nanoparticles are utilized in applications such as transistors, magnetic tools, photocatalytic processes, microelectronics, protective coatings against corrosion, electrocatalysts, and within the realm of powder metallurgy (Alahdal et al., 2023; Bordiwala, 2023; Rajeshkumar et al., 2023). The green synthesis technique utilizes different plant parts, such as roots, stems, leaves, blossoms, and seeds, for material preparation. These plant extracts contain a diverse range of phytochemicals, such as flavonoids, alkaloids, phenolic, and other bioactive compounds (Abdullah et al., 2023; Fuku et al., 2016; Hassan et al., 2020; Ijaz et al., 2017; Mayedwa et al., 2018; Phong et al., 2022; Santhoshkumar et al., 2014) characterized by the abundance of carbon, hydrogen, and nitrogen elements. Botanical extracts interacting with metal salts promote the production of nanoparticles with varying size, morphology, and surface characteristics (Awwad and Amer, 2020; Harshiny et al., 2015; Hassan et al., 2023; Jalal et al., 2023; Makarov et al., 2014; Miri et al., 2020; Shah et al., 2015; Subhapriya and Gomathipriya, 2018; Torabian et al., 2018; Vijayakumar et al., 2021).

AgNPs are a valuable substance with diverse applications in numerous industries. Notably, they exhibit elevated electrical and heat conductivity and can effectively hinder the growth of >650 species of bacteria, fungi, and algae by releasing silver ions. Silver remains inert under normal conditions in its metallic form, but it undergoes ionization when exposed to moisture from the skin and wound fluid. The resulting ionized silver becomes more reactive, binds to tissue proteins, causes structural changes in bacterial cell walls, and distorts the nuclear membrane, leading to cell death. The interaction between AgNPs and bacterial cell surfaces is particularly significant, especially in Gram-negative bacteria. Numerous studies have observed the adherence and accumulation of AgNPs on the surface of bacteria. The detrimental effects of AgNPs on cell membranes, which induce structural alternations that enhance bacterial permeability, have been extensively documented. This impact is notably influenced by factors such as nanoparticle size, shape, and concentration.

Research on *Escherichia coli* has confirmed that the accumulation of AgNPs on the cell membrane creates gaps in the bilayer's integrity, thereby increasing its permeability and resulting in bacterial cell death. Various studies have highlighted the strong correlation between the activity of AgNPs and their size (Abbasifar et al., 2017; Ahmadi, 2020; Cai et al., 2012; Du et al., 2020; Elshazly et al., 2022; Hassan et al., 2016; Panda et al., 2011; Salem and Samir, 2018; Zachar, 2020). Infected wounds pose a significant challenge in healthcare, necessitating innovative therapeutic strategies. Therefore, the current study examines the utilization of AZM-AgNPs as a promising solution to combat microbial infections in wounds. The combination of AZM-AgNPs is expected to enhance the antimicrobial efficacy while promoting wound healing.

Quinoa belongs to the Chenopodiaceae family of plants. Studies on the phytoconstituents of Quinoa seeds have identified a variety of constituents, including flavonoids, protein in the form of essential amino acids which could be reached to about 20%, carbohydrates in the form of starch (about 52–69%), lipids in the form of sulfur amino acids and

lysine (15%), and vitamins in the form of pyridoxine (B6), folic acid, vitamin E, and the antioxidant ascorbic acid (Hassan et al., 2023). Furthermore, studies done recently on the polyphenol contents in various investigations have indicated the biological activities of Quinoa seeds. Its components, which include gallic, isorhamnetin, ferulic, kaempferol, and sinapinic acids, also make Quinoa an excellent source of antioxidants for enhancing other cell activities in a variety of medical sectors (Angeli et al., 2020; Gawlik-Dziki et al., 2013). In nanoscience and technology, green synthesis offers several advantages. Using non-toxic diluters and sustainable ingredients which contain polyphenols or flavonoids that are essential for producing and processing nanoparticles, which calls for the adoption of environmentally friendly methods with no need to culture preparation or maintenance, no isolation, and economical and safe method (Krishnamoorthi et al., 2022; Malaikozhundan et al., 2022a; Malaikozhundan et al., 2022b; Malaikozhundan et al., 2020; Saddik et al., 2020b; Saddik et al., 2022b; Senthamarai and Malaikozhundan, 2022). Ag NPs were produced environmentally by using a variety of plant components (Malaikozhundan et al., 2016; Malaikozhundan et al., 2017).

There is still an urgent need for innovative therapeutic strategies to address the significant challenge posed by infected wounds in healthcare. Current treatment options often face limitations in effectively combating bacterial growth and promoting wound healing. Therefore, the development of novel pharmaceutical materials holds promise in improving treatment outcomes for infected wounds. In this study, we presented a green synthesis approach utilizing an aqueous extract of *quinoa* seeds for the eco-friendly synthesis of AgNPs. Subsequently, the incorporation of AZM onto the AgNPs' surface was investigated. The characterization of AZM-AgNPs included morphological and XRD analyses, along with investigating AZM adsorption isotherm onto the surface of the AgNPs. The antibacterial and wound-healing properties of an AZM-AgNP were assessed through in vitro antibacterial assays and in vivo experiments utilizing a rat excisional wound model.

2. Materials and methods

2.1. Materials

All reagents utilized were of analytical grade and high purity levels. Silver nitrate (AgNO3), molecular weight 169.873 g/mol, and hydroxypropylmethylcellulose (HPMC K4M) (Sigma-Aldrich, Germany) were used. The dried *quinoa* seeds were purchased from Abu Auf local market (Assuit, Egypt).

2.2. Methods

2.2.1. Preparation of aqueous solution of quinoa extracts

The aqueous extract was prepared using a previous method with slight modifications (Al-Hakkani et al., 2021c). In addition, 70 g of *quinoa* seeds were rinsed using deionized water to eliminate any impurities and adhering particles. These seeds were then dried in a hot air oven set at 110 °C to eliminate residual moisture. Using a mechanical mixer, the seeds, along with their outer layers, were ground. This resulting mixture was hydrothermally processed, reaching a concentration of 15% *w/v* in deionized water. The hydrothermal treatment included boiling and autoclaving at 121 °C and 1.1 bar pressure for 2 h. Afterward, the suspension was sieved using Whatman filter paper no. 1 and then stored in a refrigerator for subsequent use.

2.2.2. Biofabrication of adsorbent AgNPs

An anhydrous ethanolic solution containing 200 mg/L of azithromycin dihydrate working standard in absolute ethanol (AZM) was mixed with quinoa extract in the ratio (1:1) (*v*/v) with continuous stirring at a temperature of 80 °C, 1000 rpm for 6 h. The resulting precipitate was rinsed multiple times with deionized water and then centrifugated at 5000 rpm for 15 min. Subsequently, it underwent calcination at 400 °C for 2 h.

2.2.3. Adsorption of AZM on the surface of AgNPs

An anhydrous ethanolic solution of 100 mL of AZM (200 mg/L) was added to 200 mg of AgNPs with constant stirring at 350 rpm at a temperature of 303 K for 60 min. Then, the colloidal mixture was allowed to sit overnight to ensure the complete preparation of AZM-loaded AgNPs. Finally, the prepared AZM-Ag NPs were isolated from the solution through ultrafiltration using a filter with a pore size of 50 kDa.

2.2.4. Adsorption isotherm

*V*arious concentrations of 100 mL AZM (50–1000 mg/L) were examined at pH 8 using 200 mg of Ag NPs as the adsorbent to determine the optimal isothermal model for AZM adsorption onto the surface of AgNPs. The free AZM concentration was measured according to the previously reported work (Al-Hakkani, 2019c; Al-Hakkani et al., 2022b). All experiments were repeated three times, and the average values were determined following validation protocols to ensure high accuracy and precision (Al-Hakkani, 2019a, 2019b, 2019c; Al-Hakkani, 2023; Al-Hakkani et al., 2023a; Al-Hakkani et al., 2023b; Al-Hakkani et al., 2021b; Al-Hakkani et al., 2022c).

2.2.5. Determination of loading efficiency of AZM adsorbed on AgNPs

The quantification of AZM concentration loaded onto AgNPs involved directly measuring unbound AZM in the filtrate using HPLC (Al-Hakkani, 2019c). The quantity of AZM adsorbed onto AZM-AgNPs, denoted as qe (mg/g), was calculated using the following equation:

$$qe = (C_o CeV/m \quad (1)$$

where C_o and Ce represent the initial and equilibrium AZM concentrations, V is the volume of AZM in milliliters, and m is the mass of AgNPs in milligrams as the adsorbent. The loading efficiency percent (LE %) for AZM adsorption was assessed to the initial drug concentration using the formula as follows:

$$LE\% = [(C_o - Ce)/C0] \times 100 \quad (2)$$

2.2.6. Characterization of the prepared NPs

2.2.6.1. X-ray Powder Diffraction (XRD). An X-ray diffractometer (model PW 1710) equipped with a copper anode material, operating at a voltage of 40 kV and a current of 30 mA, was utilized to conduct XRD measurements for the identification of AgNPs. XRD examination was conducted utilizing a wavelength of 1.541838 Å (Cu), automatic divergence slit optics, graphite for beta filtering, and a monochromator. The samples were scanned within the angle [2θ] spectrum from 4.0° to 79°, with increments of 0.06° throughout the measurement procedure.

2.2.6.2. UV–Vis analysis. A 5 mg sample was suspended in 100 mL of deionized water to monitor the complete bioreduction of silver ions to Ag NPs. The spectrum was then captured using a UV–visible spectrophotometer scanning from 300 to 800 nm.

2.2.6.3. Transmission electron microscope (TEM). The solid samples of AgNPs and AZM-AgNPs were prepared by dispersing in ethanol, followed by precipitation onto a grid, and subsequently coated with a thin carbon film. Subsequently, the samples were allowed to dry and examined using a transmission electron microscope (JEOL model: JEM-100 CXII).

2.2.6.4. Scanning electron microscope (SEM). Each solid sample of AgNPs and AZM-AgNPs nanoparticles was affixed to double-sided carbon tape coated with a thin film of gold ranging in diameter from 150 to 200 Å. Subsequently, the samples were examined using SEM (JEOL model: JSM 5400LV) to analyze their structure and morphology.

2.2.6.5. Fourier-transform infrared spectroscopy (FTIR). FT-IR analysis was recorded on a Thermo Fisher [Nicolet iS10 FT-IR spectrometer] in a wavenumber range of 4000–500 cm-1 using a Attenuated Total Reflectance (ATR) module.

2.3. In vitro antibacterial assay

2.3.1. In-vitro antibacterial activity

The effectiveness of AZM-AgNPs was first examined using the agar diffusion technique against MRSA **(ATCC 700698, USA)**, and *E. coli* **(ATCC 25416, USA)** bacterial strains. Bacterial strains were grown on Mueller-Hinton agar plates (Oxoid, USA) at 37 °C for 18 h. A freshly made bacterial suspension was standardized to a 0.5 McFarland turbidity and spread on the surface of Mueller-Hinton agar plates. Wells with a 1 cm diameter were created utilizing a cork borer; agar samples were extracted from these wells using sterile needles. The wells were then filled with 100 μg/mL of AZM, AgNPs, AZM-AgNPs, or a saline solution (as a control). Following incubation at 37 °C, the diameters of the inhibition zones were measured (Khalid et al., 2021; Mohammed et al., 2023).

2.3.2. Preparation of azithromycin, plain AgNPs, and AZM-loaded AgNPs impregnated 2.5% w/v HPMC gels

HPMC was selected as the gelation agent at a 2.5% (*w/v*) concentration following a method described in a previous study by **(**Saddik et al., 2020a**)**. The HPMC gel was formulated by mixing the polymer with distilled water previously heated to 80 °C. The resulting blend was stirred at 1000 rpm until it became uniformly mixed. Precise amounts of 0.05% *w*/w AZM or AZM-loaded AgNPs were added to the gel, with stirring continuing until achieving an even distribution. The gels were then refrigerated at 4 °C until required.

2.3.3. Gel characterization

2.3.3.1. Tests for uniformity, pH Analysis, and Viscosity Assessment. The prepared gels were evaluated in terms of uniformity, pH, and viscosity. Following the setting of the gels in the vial, a visual inspection was conducted to assess the consistency of each gel preparation. In order to ensure the gel's uniformity required, its physical appearance and detecting the presence of any aggregates were examined. Under standard room conditions, the pH levels of pure AgNP and AZM-loaded AgNP gels were determined using a Jenway digital pH reader. The consistency of these gels was examined using a viscometer (Brookfield DV-III ultra, USA) equipped with a T-bar spindle operating at 50 rpm. The recorded viscosity was measured at a shear rate of 40 s − 1, with the gel's temperature at 30 ± 1 °C. The pH and viscosity results are depicted as the average value accompanied by the standard deviation (SD, $n = 3$).

2.3.3.2. Assessment of drug concentration in the gel. The desorption process of loaded AZM was carried out following the outlined procedure. A particular amount of AZM-loaded AgNP gel was mixed in ethanol. The gel solution in the flask underwent 15 min of vortexing, followed by an hour of sonication at room temperature to completely release the AZM. Afterward, the sample was taken out, centrifuged at 10,000 rpm, diluted as needed, and its AZM content was analyzed using the HPLC technique mentioned earlier. The results are shown as mean ± SD (n = 3).

2.3.3.3. Antimicrobial and wound healing effectiveness of laboratory animals. An infected rat model was used to investigate antimicrobial and wound-healing effects (Ekom et al., 2021). The experiments were conducted in accordance with internationally acknowledged protocols for the Care and Use of Laboratory Animals. In addition, the study's protocol was approved by the Ethics Committee of the Faculty of Pharmacy (12/1/2023/1). Twenty albino rats were divided into four sets, each containing five rats. After administering intraperitoneal thiopental anesthesia, the dorsal skin was shaved, and a 1 cm^2 circular incision was made with sterile scissors. The wound was then exposed to 10^8 colony-forming units (CFU) of MRSA. After one day, different groups were treated daily with AZM, AgNPs, and a combination of AZM-AgNPs in 2.5% HPMC gel, respectively. In contrast, the control group received only the HPMC gel without any medication. On the 7th and 10th day post-injury, photographs of the wounds were taken, and swab samples were collected at day10 post infection to test for bacterial counts. The swabs were cultured on mannitol salt agar plates and incubated at 37 °C for one day to enumerate the colony-forming units (CFU).

2.3.3.4. Histopathological evaluation. At day 10 post-injury, skin samples were excised and preserved in 10% formalin. The fixed tissues were dehydrated using a series of ethanol solutions and then embedded in paraffin. Paraffin-embedded tissues were sectioned. The hematoxylin and eosin (H&S) staining was performed according to standard protocols to visualize changes in tissue structures.

2.4. Statistical analysis

Data analysis was conducted using GraphPad Prism version 8.4 (GraphPad Software, San Diego, CA, USA). Data were represented as mean ± standard deviation (SD). To compare between groups, unpaired *t*-test was used. A p-value <0.05 was considered statistically significant.

3. Results and discussion

AgNPs were effectively synthesized using an extract derived from *quinoa* seeds, which served both as a reducing and capping agent. *Chenopodium quinoa* is considered a valuable source of antimicrobial compounds abundant in phytochemicals. The Quinoa plant's leaves and seeds extract showed a high total phenolic content, with a maximum value of 181.4 ± 1.54 (mg GAE/1 g extract) and a total flavonoid content ranging from 42.15 ± 1.21 (mg QE/1 g extract). The antimicrobial activity demonstrated a maximum inhibition zone against *S. aureus* ranging from 12 to 20 mm and against *E. coli* ranging from 10 to 18 mm (Anwar et al., 2024).

3.1. Mechanism of formation of Ag NPs

The change in color of the reaction mixture from light yellow to dark brown indicated the synthesis of Ag NPs. The process by which Ag NPs form is demonstrated in Fig. 1. Silver ions underwent reduction due to the functional groups present in plant secondary metabolites, as previously reported by Al-Hakkani (Al-Hakkani et al., 2022a, 2022b; Al-Hakkani et al., 2022c). The reduction stage included ion reduction, nucleation, and subsequent development of the nanoparticles (Al-Hakkani et al., 2022a). The bio formation of Ag NPs can be interpreted as an oxidation/ reduction reaction of aqueous Ag^+ ions mediated by the bioactive components such as flavon-3-ol, which is found in the quinoa solution (Angeli et al., 2020; Gawlik-Dziki et al., 2013; Hassan et al., 2023; Kozioł, 1992; Navruz-Varli and Sanlier, 2016; Repo-Carrasco et al., 2003; Wu, 2015).

3.2. Isothermal models study and adsorbate concentration effect

In order to determine the most appropriate model that accurately represents the interaction between the adsorbent and adsorbate, various isotherm models were applied to the data in Table 2. This was done using the linear equations formula as previously reported (Al-Hakkani et al., 2022a, 2022b).

The Langmuir isothermal model emerged as the most suitable based on its correlation coefficient, with an "R^{2}" value nearing unity at 0.9667 (Fig. 2). Moreover, the Langmuir qL value (162.73 mg/g) closely mirrored the experimental qe value (154.1 mg/g). This indicates that the

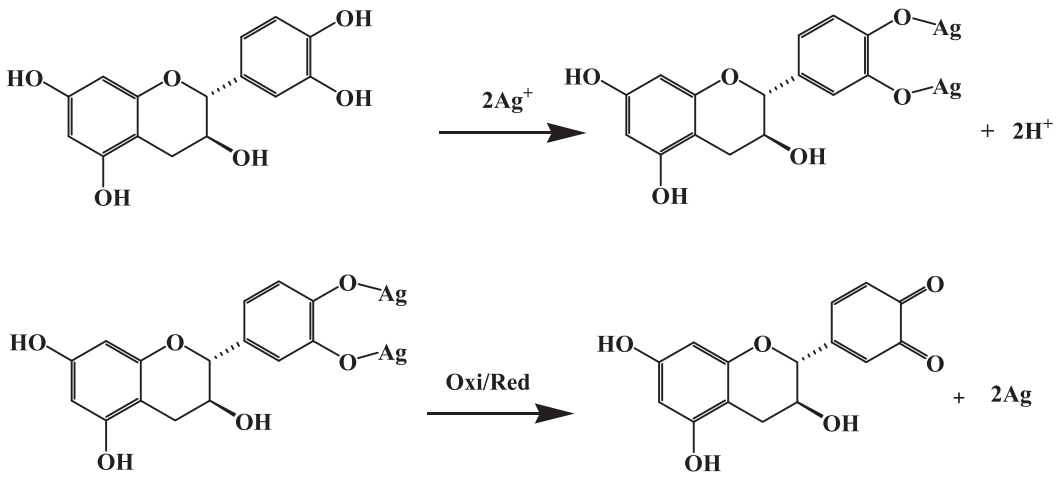

Fig. 1. Ag NPs suggested a formation mechanism via catechin in *Quinoa*.

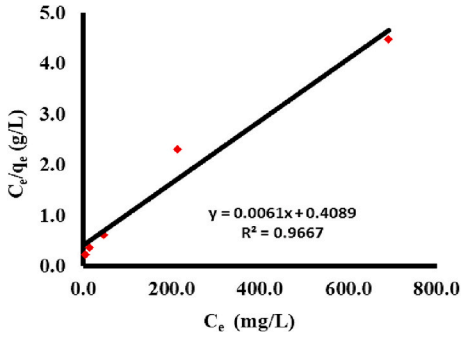

Fig. 2. Langmuir's isothermal model of AZM molecules on the surface of Ag NPs.

adsorption of AZM onto AgNP surfaces mainly resulted in the formation of a monolayer on the adsorbent surface. The consistent and uniform energy across all active binding sites on the Ag NPs indicates a homogeneous surface. The adsorption was considered favorable based on the Langmuir parameter "RL" value of 0.143, which falls between 0 and 1, specifically at 0.143 for the AZM concentration with 200 mg of Ag NPs as the adsorbent at 303 K over 60 min. Based on the data depicted in Table 1, the hierarchy of adsorption isotherm models is as follows: Langmuir > Freundlich > Temkin > D–R Model.

Utilizing various isotherm models serves a dual purpose: First, it identifies and elucidates the most precise isothermal assumption. Second, it provides crucial parameters for a better understanding of the adsorption process.

The experimental data collected were analyzed using the Temkin isotherm model. Temkin's theory suggests that "as the adsorbent mass increases, the heat of adsorption diminishes." The constant, b_T, is associated with the heat involved in the adsorption process. According to the Temkin model, a b_T value exceeding 80 kJ/mol indicates that the adsorption primarily exhibits chemisorption characteristics (Al-Hakkani et al., 2022a, 2022b). In our study, the b_T was found to be 99.4.

Table 1
Analyzed isothermal data using different applied models.

Item	Isothermal models			
	Langmuir	Freundlich	Temkin	D-R
R^2	0.9667	0.9513	0.9462	0.7112
Model parameter	$q_L = 162.73$	$n = 2.7$	$B_T = 25.3$	$q_{D\text{-}R} = 88.28$
	$k_L = 0.015$	$k_F = 14.2$	$A_T = 0.376$	$\beta = -7.64 \times 10^{-6}$
	$R_L = 0.143$		$b_T = 99.4$	$E_{D\text{-}R} = 255.83$

The Freundlich model can confirm the suitability and desirability of the adsorption process by ensuring that the n parameter falls within the range of 1–10 (Al-Hakkani et al., 2022a, 2022b). The n value was determined to be 2.7, while the reciprocal of n was 0.371, indicating that the adsorption was significant. These findings indicate that the adsorption process deviated from the Freundlich model's assumption, which posits heterogeneous surface energy for binding sites and reversible adsorption in multilayer structures. The elevated kF value of 14.2 mg/g highlights a significant adsorption capacity (Ou et al., 2015).

In a previous study by (Saddik et al., 2022a), it was determined that the adsorption of AZM onto zinc oxide nanoparticles adheres to the Freundlich adsorption model, with a correlation coefficient of kF = 5.6. In our study, the correlation coefficient (representing adsorption capacity) exhibited a more significant correlation compared to zinc oxide, with a value of kF = 14.2. The evidence demonstrates that the AZM molecules are more closely bound to the nanostructure in the current approach than in the previous manuscript, making them more effective than what was shown with ZnO nanostructures. Furthermore, the bond strength between the surface of the nano-adsorbent material and the adsorbed material (AZM) on its surface becomes more robust as the reciprocal of the factor n approaches zero (Al-Hakkani et al., 2022a; Hassan et al., 2023). The study showed a difference between the two values, as it was higher in the case of the association of AZM with zinc oxide nanoparticles (0.541) than in the case of the adsorption of AZM on the AgNP surface in the current approach (0.371).

When comparing the Langmuir-type adsorption model, the current approach yielded a higher value for the adsorbed layer of AZM (162.73 mg/g) compared to the previous study (160.44 mg/g), indicating that the current approach provides better results in the context of wound healing using the trade-off model. The higher adsorption capacity observed in the current study with AgNPs compared to ZnO nanoparticles in previous research is attributed to the smaller particle size of the adsorbent surface and the larger surface area available for the adsorption process. The average crystallite size by XRD was 38 nm for ZnO nanoparticles, whereas for AgNPs, it was 27.3 nm (Al-Hakkani et al., 2021c). This finding is is attributed to the utilization of quinoa plant extract in nanoparticle preparation processes in the current approach (Hassan et al., 2023).

The D-R isothermal model was also examined, yielding the average adsorption energy for each AZM molecule bound to Ag NPs, referred to as "free energy ($E_{D\text{-}R}$)," which was determined to be 255.83. Given that this $E_{D\text{-}R}$ value exceeds 80, it suggests that the adsorption predominantly exhibits chemisorption characteristics (Davoodi et al., 2019).

Fig. 3 demonstrates variations in the adsorption of AZM by AgNPs at various concentrations. The adsorption capacity demonstrated a

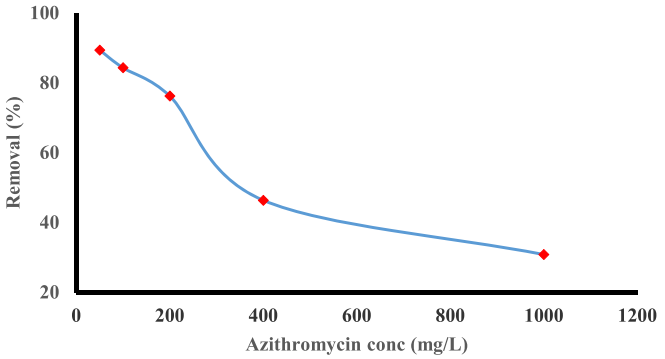

Fig. 3. Percent of AZM removal by AgNPs at different AZM.

significant decline in removal percentage, shifting from 89.4% to 84.3% as the AZM concentration transitioned from 50 mg/L to 100 mg/L. Adsorption capacities decreased as concentrations increased beyond 100 mg/L, reaching 76.2%. There was a notable and sudden decrease in the removal of AZM, with removal percentages decreasing as follows: 89.4% → 84.3% → 76.2% → 46.4% → 30.8%. This indicates that the optimal adsorbate concentration for AZM stands at 200 mg/L.

3.3. XRD analysis

As depicted in Fig. 4, all the reflection peaks (2θ) are closely aligned with the reference card ICDD # 00–901-3046, representing pure silver metal in a cubic crystal structure.

The crystallite size ("Dscher") for each distinctive silver peak, determined by applying the Scherrer equation to the corresponding Two Theta values, is presented in Table 2.

Instrumental broadening and sample interactions lead to widening peaks in the Bragg phenomenon. The full widths at half maximum (FWHM) of the detected peaks were calculated and modified using the Pseudo-Voigt function (Madhu et al., 2013). This line profile relationship can be expressed by the eq. (1) as follows:

$$\beta_{hkl} = \left[\beta^2_{mes.} - \beta^2_{inst.}\right]^{1/2} \quad (3)$$

where β_{hkl} is the corrected FWHM, $\beta_{mes.}$ is the measured FWHM, and $\beta_{inst.}$ is the instrumental FWHM.

The Scherrer equation (Alahmadi et al., 2023; Mohamed and Abu-Dief, 2018) can be used to calculate the average crystallite size as follows:

$$D_{scher} = 0.9\lambda/\beta_{hkl}\, cos(\theta_{hkl}) \quad (4)$$

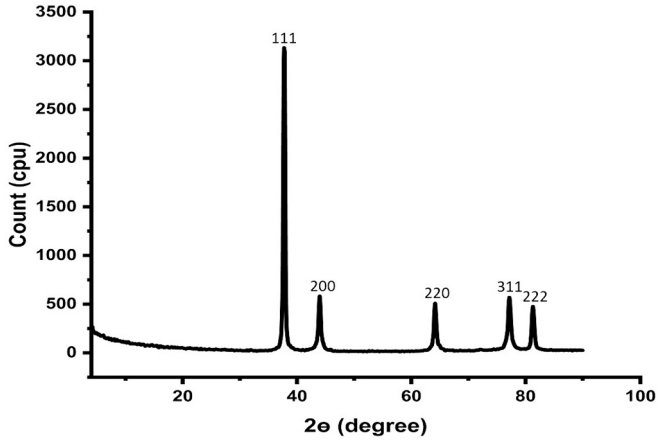

Fig. 4. X-ray diffractogram of the as-biofabricated AgNPs.

Table 2
Structural XRD parameters of the as-prepared *AgNPs*.

Parameter	AgNPs				
λ (nm)			0.1541838		
Miller indices (hkl)	111	200	220	311	222
Reference (2θ)	37.8945	44.0391	64.0384	76.8874	80.9879
$2\theta_{mes.}$	37.72	43.96	64.18	77.14	81.28
$\theta_{mes.}$ in degree	18.8600	21.9800	32.0900	38.5700	40.6400
$\theta_{mes.}$ in radian	0.3292	0.3836	0.5601	0.6732	0.7093
Gaussian $FWHM_{mes.}$ ($\beta_{mes.}$) in degree	0.4016	0.3818	0.3569	0.3896	0.3729
Gaussian $FWHM_{mes.}$ ($\beta_{mes.}$) in radian	0.0070	0.0067	0.0062	0.0068	0.0065
$FWHM_{inst.}$ ($\beta_{inst.}$) in degree			0.16		
$FWHM_{inst.}$ ($\beta_{inst.}$) in radian			0.002792527		
Gaussian β_d = sqrt ($(\beta^2_{mes.} - \beta^2_{inst.})$) in radian	0.0064	0.0061	0.0056	0.0062	0.0059
$Sin\theta_{mes.}$	0.3233	0.3743	0.5313	0.6235	0.6513
$Cos\theta_{mes.}$	0.9463	0.9273	0.8472	0.7818	0.7588
Gaussian D_{scher} (nm)	22.8	24.7	29.4	28.6	31.1
Gaussian Average D_{scher} (nm)			27.3		
$d_{mes.}$ (Å)	2.3848	2.0597	1.4511	1.2365	1.1837
Reference d (Å)	2.3723	2.0545	1.4528	1.2389	1.1862

As shown in the pattern of Fig. 2, there are no distinct diffraction peaks or other indicators suggesting that the biosynthesized silver is in an amorphous crystalline state. The crystalline nature of the biosynthesized Ag NPs is confirmed by the clarity of the primary reflected peaks (Al-Hakkani et al., 2022a, 2022b; Al-Hakkani et al., 2022c). Additionally, smaller particle sizes tend to exhibit a higher degree of crystallinity (Aisida et al., 2020; Amaliyah et al., 2020; Anchan et al., 2019; Harshiny et al., 2015; Hassan et al., 2023; Kaur et al., 2019; Onyedikachi et al., 2022; Vembu et al., 2022; Wang et al., 2007).

3.4. UV–Vis analysis

To examine the complete bioreduction of silver ions to AgNPs, 5 mg of the sample was suspended in 100 mL of deionized water, and a UV–visible spectrophotometer was employed to capture the sample's spectrum over a scanning range of 300 to 800 nm. As shown in Fig. 5, the AgNPs displayed a single absorption peak in the UV spectrum at a specific nm, aligning with the findings of (Elshazly et al., 2022). The

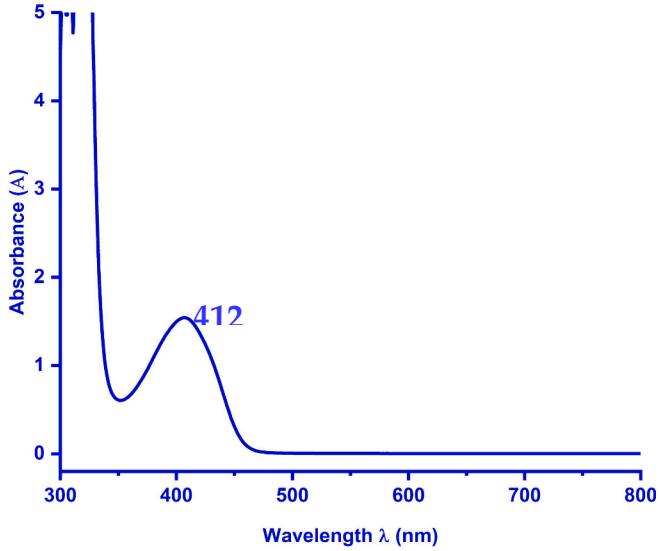

Fig. 5. UV–Vis absorption spectrum of the as-prepared *AgNPs*.

stability of the freshly prepared AgNPs was assessed over 14 days in a suspended state in distilled water, with continuous monitoring of the distinct absorption peak in the spectrum.

3.5. SEM and TEM analysis

The properties and applications of nanoparticles are mainly dependent on their size and shape. Smaller nanoparticles have a significantly larger specific surface area, making them well-suited for use in cancer treatment and bacterial inhibition. The scanning electron microscope (SEM) images of the synthesized AgNPs displayed consistent semi-spherical and cubic configurations. This morphology could be attributed to bioactive molecules adhering to the AgNPs, confirming the encapsulating role of the *quinoa* components around the developed NPs, as demonstrated in Fig. 6a.

The TEM visualization of the Ag NPs in Fig. 6b depicts particles with both spherical and cubic geometries, appearing as distinct dark spots dispersed without notable clumping. Upon analyzing the particle size data, the average dimension of the AgNPs was 24.9 ± 15.2 nm. As shown in Fig. 6c, the size distribution histogram was further specified, with sizes ranging from a minimum of 6.4 nm to a maximum of 66.9 nm, with a median measurement of 19.6 nm.

Fig. 6d shows the surface of the Ag NPs after loading, where the AZM molecules were adsorbed and formed an adsorbed layer. Fig. 6e **&** Fig. 6f depict the TEM image and particle size distribution. The average size of AZM-Ag NPs is 34.7 ± 9.7 nm, indicating a significant increase in particle size. The smallest particle recorded was 14.9 nm, the largest was 53.9 nm, and the histogram's median size was 34.6 nm.

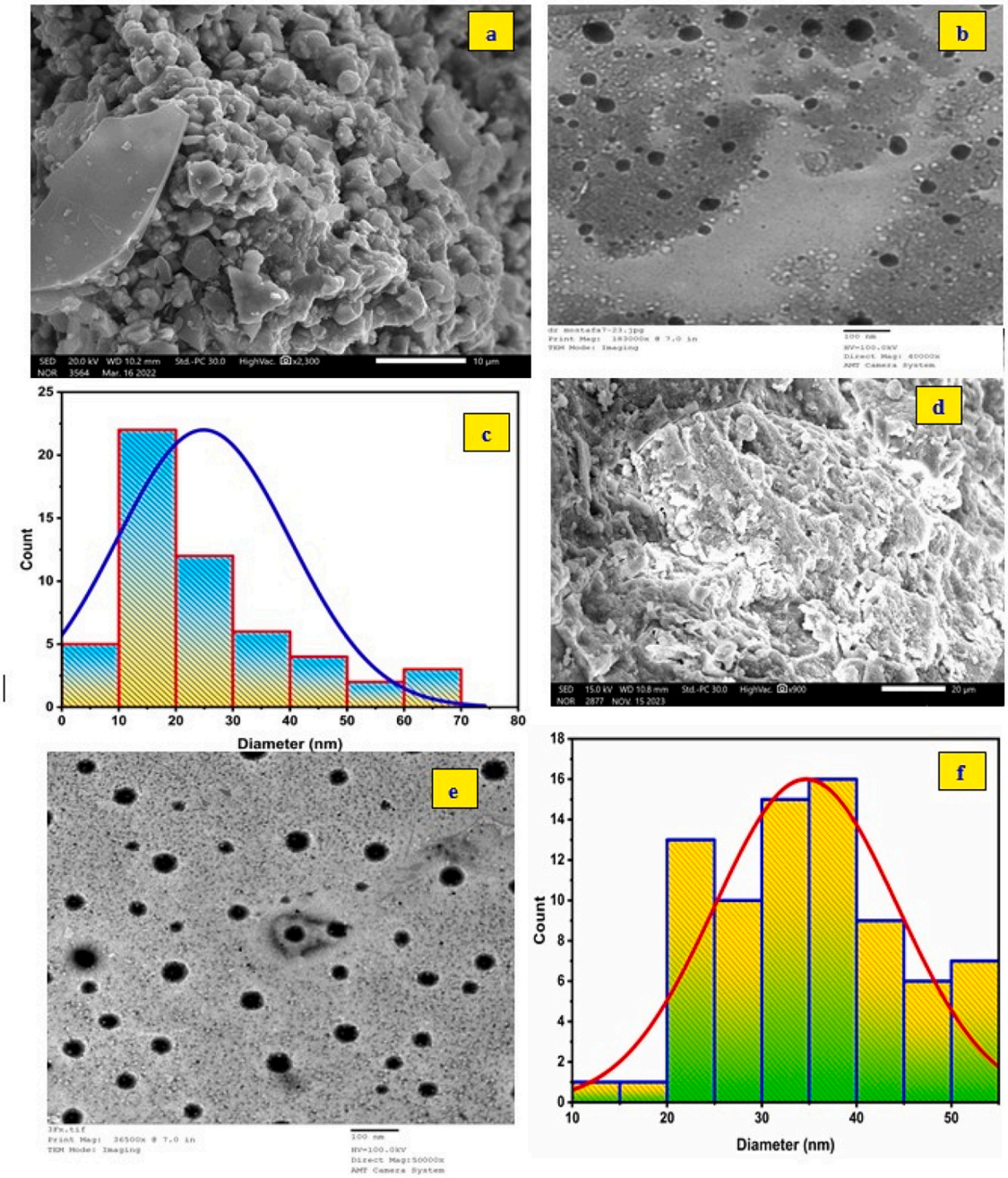

Fig. 6. The as-prepared *Ag NPs* befor adsorption process a) SEM image, b) TEM image, and c) Particle size distribution, and after adsorption process d) SEM image, e) TEM image, and f) Particle size distribution.

3.6. FTIR analysis

The most effective method for determining and verifying the presence of potential functional groups in the bioactive components that are in charge of the reduction process of the copper metal ions is FTIR analysis (Al-Hakkani, 2020; Al-Hakkani et al., 2021a). The confirmation of some functional groups' involvement in the capping-stabilization role of the as-biosynthesized Ag NPs is another crucial function of FTIR investigation. The primary factor for the metal ion reduction in biosynthesized silver nanoparticles might be these bioactive chemicals. Certain bands in the extract were missing or altered from before the reaction after the bioreduction procedure. This might be explained by the presence of bioactive compounds in the plant extract that are engaged in the bioreduction process, such as flavonoids or polyphenols (Saddik et al., 2020b).

As seen in Fig. 7, the Quinoa seeds powder's abundance of functional groups such as -OH at 3291 cm^{-1}, -CH at 2918, 2848 cm^{-1}, -CN at 2166 cm^{-1}, C═O at 1617 cm^{-1}, and -OH at 1023 cm^{-1} play a crucial part in the processes of bioreduction, stabilization, and capping which appeared in the biosynthesized Ag NPs with some deviations in the wavenumbers.

After the adsorption process of the AZM onto the Ag NPs, some of AZM functional groups enable further interaction between the Ag NPs and certain of the substances by being adsorbed at their surface. Double bonds, hydrogen bonds, or electrostatic contact may be responsible for these NPs' additional interaction.

3.7. In vitro antibacterial activities

The agar diffusion technique was employed to assess the antibacterial efficacy of the formulations. The mean diameters of the inhibition zones correspond to the AZM's unbound formulation. Specifically, a 100 µg/mL concentration of unbound AZM yielded inhibition zones of approximately 14 ± 4 mm and 11.7 ± 3 mm, targeting MRSA and *E. coli*, respectively. In contrast, AZM-AgNPs at the same concentration resulted in zones measuring 23 ± 5 mm and 16 ± 3 mm targeting *E. coli* and MRSA, underscoring a heightened antibacterial potency (Fig. 8). Furthermore, the Minimum Inhibitory Concentrations (MICs) for both the free drug and the nanoformulation were determined. Notably, the MIC for AZM was markedly decreased from 22 µg/mL to 13 µg/mL against MRSA and from 34 µg/mL to 18 µg/mL against *E. coli* in the AZM-AgNPs formulation (Table 3).

3.8. Characterization of blank AgNPs and AZM-AgNPs gel

Both the AgNP gel without AZM and AZM-loaded AgNPs were assessed for uniformity, pH level, and viscosity. Both formulations displayed a uniform texture with no clumps or aggregations. The pH of these gels fell within the range of 4 to 6, which is considered suitable for avoiding skin irritation when applied. It is widely recognized that skin-applied products should maintain a pH between 4 and 6 to minimize the chances of skin irritation. This aligns with human skin's natural acidic pH range, typically between 4.1 and 5.8 (Proksch, 2018). Moreover, the pH values of the two gels did not show any significant difference, as shown in Table 4. The thickness of the produced gels was also gauged, and the specifics are detailed in Table 4. The AZM concentration in the AZM-loaded AgNPs was measured at 97.87 ± 2.03, falling within the established standard limits. This result indicates a consistent and even distribution of the AZM drug within the AgNPs-HPMC gel.

3.9. In vivo activity of the formulation

In order to evaluate the in vivo antimicrobial and wound healing characteristics of the formulations, daily treatments were administered to four distinct groups of injured rats: AZM (Group I), AgNPs (Group II), AZM-AgNPs (Group III), and the control group (Group IV) treated with an unmedicated gel. On the seventh and tenth day post-infection, the animals were photographed in order to visually document the effects of AZM-AgNP treatment (Fig. 9A). Compared with the other treated groups, Group III exhibited a more rapid recovery of wounds, as indicated by significant wound contraction and enhanced healing. Furthermore, it was observed that Group III had a more favorable skin appearance and consistent hair growth than the other treated groups, which displayed reduced healing.

Furthermore, bacterial counts in wounds treated with AZM, AgNPs, or AZM-AgNPs (log CFU = 4.9 ± 0.8, 5.9 ± 0.6 and 2.4 ± 1.3, respectively) were significantly lower by day 10 post-infection, when compared to the control group (log CFU = 7.3 ± 0.3). The bacterial reduction in Group III, treated with the AZM-AgNPs-impregnated HPMC gel, was notably more prominent compared to the reductions observed

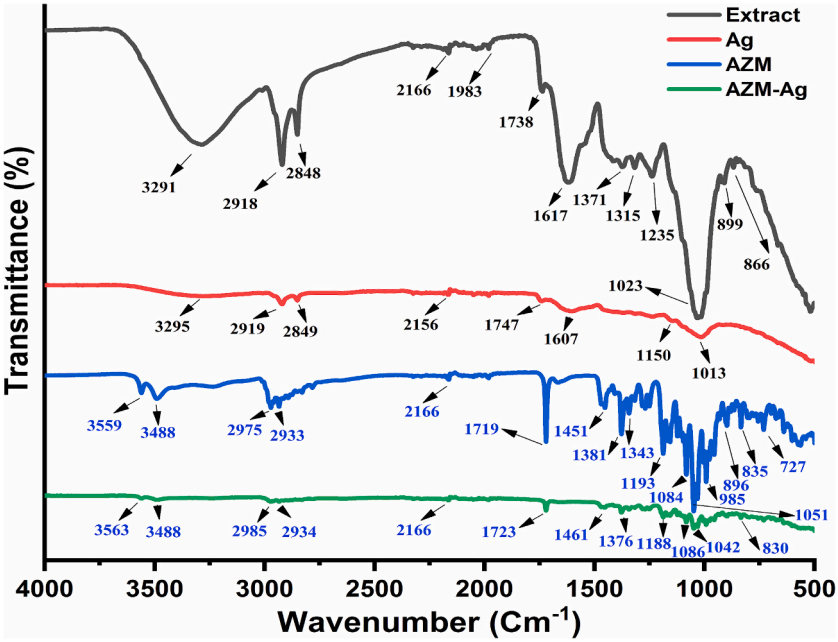

Fig. 7. FTIR spectra of the *Quinoa* extract, the as-biofabricated *Ag NPs, AZM, and AZM-Ag.*

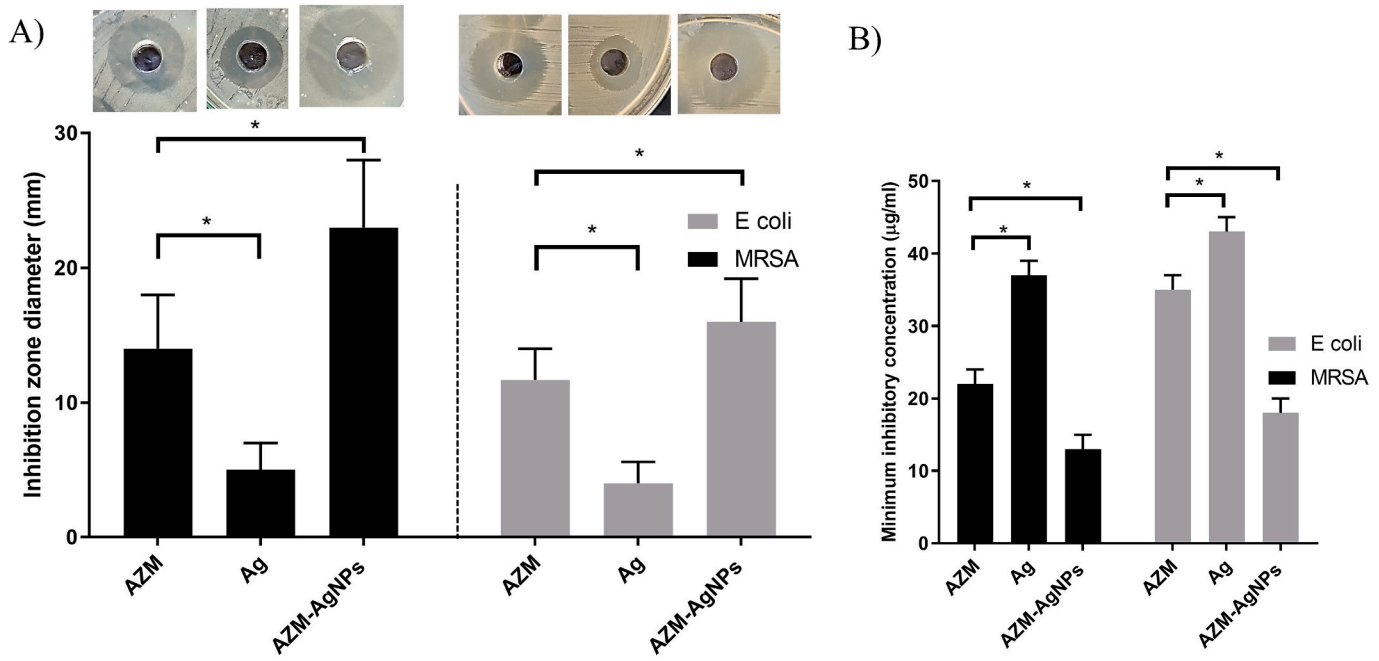

Fig. 8. AZM-loaded AgNPs exhibit enhanced antibacterial efficacy. A) depicts the average sizes of inhibition zones caused by AZM, AgNPs, and AZM-AgNPs on agar plates containing MRSA and *E. coli* cultures, accompanied by a sample image for each treatment. B) presents the MIC for AZM, AgNPs, and AZM-AgNPs directed against MRSA and *E. coli*. Data are presented as the mean ± standard deviation of at least three experiments. Groups were compared using unpaired *t*-test. *; denote significance.

Table 3
MIC of the tested formulations against MRSA and E coli strains.

Bacteria	AZM	Ag	AZM-AgNPs
MRSA	22 µg/mL	37 µg/mL	13 µg /mL
E coli	34 µg/mL	43 µg/mL	18 µg /mL

Table 4
Viscosity, pH, and drug content parameters of Blank Ag NPs gel and AZM - Ag NPs.

Gel	Viscosity centipoise x10^2	pH	Drug content (%)
Blank AgNPs	24.32 ± 1.46	5.62 ± 0.4	–
AZM - AgNPs	24.11 ± 1.93	5.73 ± 0.3	97.87 ± 2.03

in the other treatment groups. AZM-AgNPs treatment was associated with 67.1% reduction in bacterial counts ($p < 0.001$), while AZM and AgNP treatment reduced bacterial counts by 38.4% and 19.2% (*P* values <0.01 and 0.02, respectively), as shown in Fig. 8B.

3.10. Histopathological analysis of the skin layers treated with the different formulations

The histological evaluation of skin samples from four experimental groups revealed significant differences in wound healing outcomes. The control group exhibited marked discretion of epidermis, delayed epithelialization, and reduced granulation tissue. In contrast, rats treated with AZM displayed moderate improvement with enhanced epithelialization and increased granulation tissue formation. The AgNPs group demonstrated effects on these parameters, displaying varying degrees of improvement. Notably, the group receiving AZM-loaded AgNPs exhibited the most favorable outcomes, characterized by superior epithelialization and robust granulation tissue formation. Furthermore, it enhanced collagen deposition, surpassing the individual effects of AZM or AgNPs alone and highlighting the potential synergistic effects of AZM and AgNPs on wound healing in this rat model (Fig. 10).

4. Conclusions

In conclusion, the formulation and evaluation of azithromycin-loaded silver nanoparticles (AZM-AgNPs) present a promising therapeutic approach for the treatment of infected wounds. Through the utilization of green synthesis methods with Quinoa seed extract, we successfully synthesized AgNPs and loaded them with azithromycin. Characterization techniques including XRD, SEM, TEM, and UV–Vis analysis confirmed the successful synthesis and loading of azithromycin onto silver nanoparticles. The agar diffusion assay and determination of MIC demonstrated the potent antibacterial activity of AZM-AgNPs against both MRSA and *E. coli*. Furthermore, in vivo studies conducted on infected rat models revealed enhanced wound healing and reduced bacterial counts in AZM-AgNP treated rats compared to the control group. These findings highlight the potential of AZM-AgNPs as an effective therapeutic agent for the management of infected wounds, offering a great approach to combat bacterial growth and improve wound healing outcomes in clinical settings. Further research and clinical trials are warranted to validate the efficacy and safety of AZM-AgNPs or dressings infused with AZM-AgNPs for broader clinical applications, such as the management of chronic diabetic wounds in clinical settings.

Author contributions

Conceptualization: M.S.S., M.F.Al-H. and M.H.A.H; methodology: M.S.S., M.S.M., A.M.A., I.A.A., M.M., M.K.M., M.H.A.H., M.F.Al-H., M.A.S. and M.A.E.-M. Software: M.S.S., M.F.Al-H., M.K.M.; formal analysis: M.S.S., A.M.A. and M.F.Al-H.; investigation: M.S.S., M.F.Al-H., A.M.A. and H.A.A.; writing-original draft preparation: M.K.M., M.S.S., M.S.M., M.A.S., M.F.Al-H.,A.M.A., I.A.A., M.M. and M.H.A.H.; writing-review and editing: M.K.M., M.S.S., M.A.S., M.F.Al-H., A.M.A., M.H.A.H, M.A.E.-M., K.AL-G. and M.S.A. supervision: M.S.S., A.M.A. and M.F.Al-H project administration: M.S.S., M.H.A.H. and M.F.Al-H. funding acquisition: A.

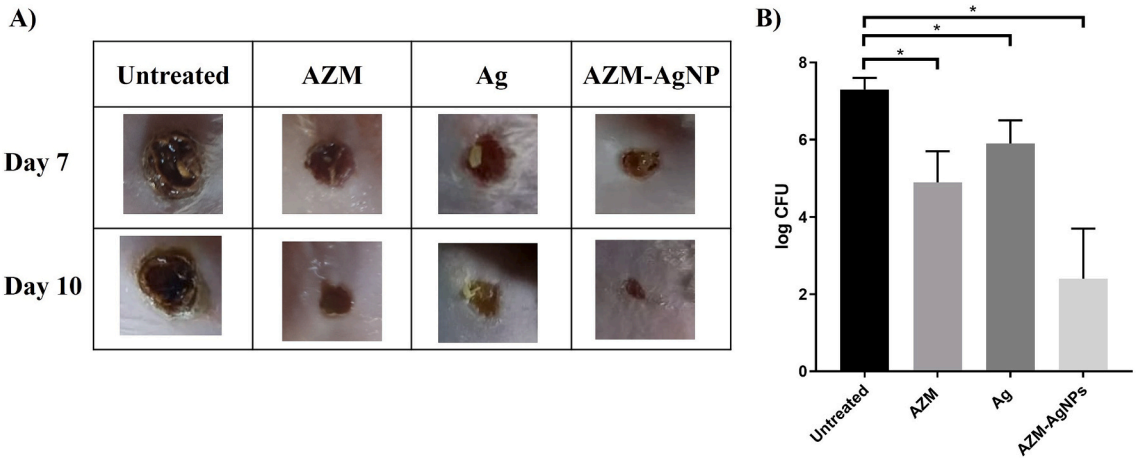

Fig. 9. In vivo evaluation of the examined formulations. A) Rats' injuries were exposed to MRSA, followed by treatment with specified formulations. Images were captured on the 7th and 10th days after infection to monitor the healing process. B) On the 10th day following the infection, the bacterial concentration in the damaged skin was analyzed. The outcomes are depicted as average values with standard deviations. CFU stands for colony forming units. Data are presented as the mean ± standard deviation. Groups were compared using unpaired *t*-test. *; denote significance.

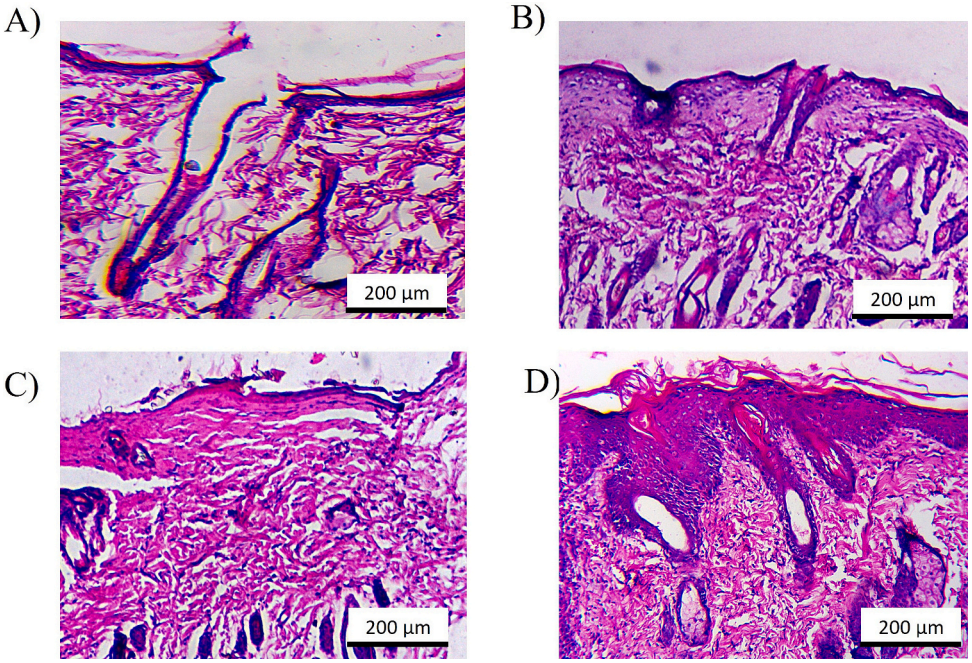

Fig. 10. Histological Sections of Rat Skin Wounds in Various Treatment Groups. (a) Control group showing marked tissue destruction and delayed healing. (b) The Azithromycin (AZM) group demonstrates enhanced epithelialization and increased granulation tissue formation. (c) The AgNPs group shows lower degrees of improvement. (d) The AZM-AgNP combination group exhibits the most favorable outcomes, characterized by superior epithelialization and robust granulation tissue formation, surpassing the individual effects of AZM or AgNPs alone.

M.A., M.S.A., H.A.A., and K.AL-G.; data curation: M.S.S., M.K.M., M.M., M.F.Al-H., M.S.M., I.A.A., M.H.A.H., M.A.S., M.S.A., K.ALG., H.A.A. and M.A.E.M, method validation: M.S.S., M.F.Al-H., A.M.A., I.A.A., M.M., M. H.A.H. and M.S.M.

All authors have read and agreed to the published version of the manuscript.

Funding

This research was funded by [Ministry of Education in Saudi Arabia] with grant number [445-9-765].

Institutional review board statement

The research adhered to the principles of the Declaration of Helsinki and received approval from the Institutional Ethics Committee of the Faculty of Pharmacy at Sohag University (12/1/2023/1).

Informed consent statement

Not applicable.

CRediT authorship contribution statement

Mostafa F. Al-Hakkani: Writing – review & editing, Writing –

original draft, Validation, Software, Investigation. **Ahmed M. Abu-Dief:** Writing – original draft, Validation, Supervision, Resources, Methodology, Formal analysis, Conceptualization. **Mohamed S. Mohamed:** Supervision, Project administration, Funding acquisition, Conceptualization. **Islam A. Al-Fattah:** Project administration, Funding acquisition, Formal analysis, Data curation. **Mahmoud Makki:** Software, Project administration, Investigation, Conceptualization. **Mohamed A. El-Mokhtar:** Supervision, Project administration, Conceptualization. **Marwa A. Sabet:** Validation, Resources, Formal analysis, Conceptualization. **M.S. Amin:** Writing – review & editing, Writing – original draft, Visualization, Software, Methodology, Funding acquisition, Conceptualization. **Hoda A. Ahmed:** Resources, Methodology, Data curation. **Khalaf Al-Ghamdi:** Funding acquisition, Data curation. **Mostafa K. Mohammad:** Writing – original draft, Visualization. **Mohammad H.A. Hassan:** Project administration, Investigation, Formal analysis.

Declaration of competing interest

The authors declare that they have no known competing financial interests or personal relationships that could have appeared to influence the work reported in this paper.

Data availability statement

The data produced and analyzed in this study can be obtained from the corresponding authors upon a reasonable request.

Acknowledgments

The authors express their gratitude to the Deputyship for Research and Innovation, Ministry of Education in Saudi Arabia, for funding this research work under project number 445-9-765.

References

Abbasifar, A., Ghani, S., Irvani, M.A., Rafiee, B., Kaji, B.V., Akbari, A., 2017. Antibacterial activity of silver nanoparticles synthesized by using extracts of *Hedera helix*. Zahedan J. Res.Med. Sci. 19.

Abdullah, M., Iqbal, J., Ur Rehman, M.S., Khalid, U., Mateen, F., Arshad, S.N., Al-Sehemi, A.G., Algarni, H., Al-Hartomy, O.A., Fazal, T., 2023. Removal of ceftriaxone sodium antibiotic from pharmaceutical wastewater using an activated carbon based TiO2 composite: Adsorption and photocatalytic degradation evaluation. Chemosphere 317, 137834.

Abu-Dief, A.M., Abdel-Rahman, L.H., Abd-El Sayed, M.A., Zikry, M.M., Nafady, A., 2020. Green synthesis of AgNPs ultilizing Delonix Regia extract as anticancer and antimicrobial agents. ChemistrySelect 5 (42), 13263–13268.

Abu-Dief, A.M., Abdel-Rahman, L.H., Sayed, M.A.E., Zikry, M.M., Khalifa, M.E., El-Metwaly, N.M., 2022. Optimization strategy for green synthesis of silver nanoparticles (AgNPs) as catalyst for the reduction of 2, 4-dinitrophenol via supported mechanism. Appl. Phys. A 128 (7), 595.

Ahmadi, S., 2020. The importance of silver nanoparticles in human life. Adv. Appl. NanoBio-Technol. 1, 5–9.

Aisida, S.O., Madubuonu, N., Alnasir, M.H., Ahmad, I., Botha, S., Maaza, M., Ezema, F.I., 2020. Biogenic synthesis of iron oxide nanorods using Moringa oleifera leaf extract for antibacterial applications. Appl. Nanosci. 10, 305–315.

Alahdal, F.A., Qashqoosh, M.T., Manea, Y.K., Mohammed, R.K., Naqvi, S., 2023. Green synthesis and characterization of copper nanoparticles using Phragmanthera austroarabica extract and their biological/environmental applications. Sustain. Mater. Technol. 35, e00540.

Alahmadi, M., Alsaedi, W.H., Mohamed, W.S., Hassan, H.M., Ezzeldien, M., Abu-Dief, A. M., 2023. Development of Bi_2O_3/$MoSe_2$ mixed nanostructures for photocatalytic degradation of methylene blue dye. J. Taibah University for Sci. 17 (1), 2161333.

Al-Hakkani, M.F., 2019a. Forced degradation study with a developed and validated RP-HPLC method for determination of cefpodoxime proxetil in the bulk and finished pharmaceutical products. J. Iran. Chem. Soc. 16, 1571–1578.

Al-Hakkani, M.F., 2019b. Guideline of inductively coupled plasma mass spectrometry "ICP–MS": fundamentals, practices, determination of the limits, quality control, and method validation parameters. SN Appl. Sci. 1, 791.

Al-Hakkani, M.F., 2019c. A rapid, developed and validated RP-HPLC method for determination of azithromycin. SN Appl. Sci. 1, 222.

Al-Hakkani, M.F., 2020. Biogenic copper nanoparticles and their applications: a review. SN Appl. Sci. 2, 505.

Al-Hakkani, M.F., 2023. A new validated facile HPLC analysis method to determine methylprednisolone including its derivatives and practical application. Sci. Rep. 13, 11548.

Al-Hakkani, M.F., Gouda, G.A., Hassan, S.H.A., 2021a. A review of green methods for phytofabrication of hematite (α-Fe_2O_3) nanoparticles and their characterization, properties, and applications. Heliyon 7, e05806.

Al-Hakkani, M.F., Gouda, G.A., Hassan, S.H.A., Farghaly, O.A., Mohamed, M.M.A., 2021b. Fully investigation of RP- HPLC analytical method validation parameters for determination of Cefixime traces in the different pharmaceutical dosage forms and urine analysis. Acta Pharm. Sci. 59, 97–111.

Al-Hakkani, M.F., Gouda, G.A., Hassan, S.H.A., Nagiub, A.M., 2021c. *Echinacea purpurea* mediated hematite nanoparticles (α-HNPs) biofabrication, characterization, physicochemical properties, and its in-vitro biocompatibility evaluation. Surf.Interf. 24, 101113.

Al-Hakkani, M.F., Gouda, G.A., Hassan, S.H.A., Mohamed, M.M.A., Nagiub, A.M., 2022a. Cefixime wastewater management via bioengineered Hematite nanoparticles and the in-vitro synergetic potential multifunction activities of Cefixime@Hematite nanosystem. Surf.Interf. 30, 101877.

Al-Hakkani, M.F., Gouda, G.A., Hassan, S.H.A., Mohamed, M.M.A., Nagiub, A.M., 2022b. Environmentally azithromycin pharmaceutical wastewater management and synergetic biocompatible approaches of loaded azithromycin@hematite nanoparticles. Sci. Rep. 12, 10970.

Al-Hakkani, M.F., Gouda, G.A., Hassan, S.H.A., Saddik, M.S., El-Mokhtar, M.A., Ibrahim, M.A., Mohamed, M.M.A., Nagiub, A.M., 2022c. Cefotaxime removal enhancement *via* bio- nanophotocatalyst α-Fe_2O_3 using photocatalytic degradation technique and its echo-biomedical applications. Sci. Rep. 12, 11881.

Al-Hakkani, M.F., Ahmed, N., Abbas, A.A., Hassan, M.H.A., 2023a. Cefoperazone rapidly and sensitive quantitative assessment via a validated RP-HPLC method for different dosage forms, in-use stability, and antimicrobial activities. BMC Chem. 17, 72.

Al-Hakkani, M.F., Ahmed, N., Hassan, M.H.A., 2023b. Rapidly, sensitive quantitative assessment of thiopental via forced stability indicating validated RP-HPLC method and its in-use stability activities. Sci. Rep. 13, 10294.

Amaliyah, S., Pangesti, D.P., Masruri, M., Sabarudin, A., Sumitro, S.B., 2020. Green synthesis and characterization of copper nanoparticles using Piper retrofractum Vahl extract as bioreductor and capping agent. Heliyon 6, e04636.

Anchan, S., Pai, S., Sridevi, H., Varadavenkatesan, T., Vinayagam, R., Selvaraj, R., 2019. Biogenic synthesis of ferric oxide nanoparticles using the leaf extract of Peltophorum pterocarpum and their catalytic dye degradation potential. Biocatal. Agric. Biotechnol. 20, 101251.

Angeli, V., Miguel Silva, P., Crispim Massuela, D., Khan, M.W., Hamar, A., Khajehei, F., Graeff-Hönninger, S., Piatti, C., 2020. Quinoa (Chenopodium quinoa Willd.): an Overview of the Potentials of the "Golden Grain" and Socio-Economic and Environmental Aspects of its Cultivation and Marketization. Foods 9, 216.

Anwar, H., Habib, A., Taj, M.U., Ali, M.A., Munir, A., Shafi, M., Saddique, M., Ahmed, S., Coutinho, H.D.M., 2024. Phytochemical Screening and Antimicrobial Potential of *Chenopodium quinoa* Extract against Pathogenic Bacterial Strains (Vegetos).

Awwad, A., Amer, M., 2020. Biosynthesis of copper oxide nanoparticles using Ailanthus altissima leaf extract and antibacterial activity. Chem. Int. 6, 210–217.

Bordiwala, R.V., 2023. Green Synthesis and Applications of Metal Nanoparticles.-A Review article. Results in Chemistry, p. 100832.

Bowler, P., Duerden, B., Armstrong, D.G., 2001. Wound microbiology and associated approaches to wound management. Clin. Microbiol. Rev. 14, 244–269.

Buarki, F., AbuHassan, H., Al Hannan, F., Henari, F.Z., 2022. Green Synthesis of Iron Oxide Nanoparticles using Hibiscus rosa sinensis Flowers and their Antibacterial activity. J. Nanotechnol. 2022, 5474645.

Cai, X., Lin, M., Tan, S., Mai, W., Zhang, Y., Liang, Z., Lin, Z., Zhang, X., 2012. The use of polyethyleneimine-modified reduced graphene oxide as a substrate for silver nanoparticles to produce a material with lower cytotoxicity and long-term antibacterial activity. Carbon 50, 3407–3415.

Davoodi, S., Dahrazma, B., Goudarzi, N., Gorji, H.G., 2019. Adsorptive removal of azithromycin from aqueous solutions using raw and saponin-modified nano diatomite. Water Sci. Technol. 80, 939–949.

Du, T., Zhang, J., Li, C., Song, T., Li, P., Liu, J., Du, X., Wang, S., 2020. Gold/Silver Hybrid Nanoparticles with Enduring Inhibition of Coronavirus Multiplication through Multisite Mechanisms. Bioconjug. Chem. 31, 2553–2563.

Ekom, S.E., Tamokou, J.-D.-D., Kuete, V., 2021. Antibacterial and therapeutic potentials of the Capsicum annuum extract against infected wound in a rat model with its mechanisms of antibacterial action. Biomed. Res. Int. 2021, 1–17.

Elshazly, E.H., Mohamed, A.K.S.H., Aboelmagd, H.A., Gouda, G.A., Abdallah, M.H., Ewais, E.A., Assiri, M.A., Ali, G.A.M., 2022. Phytotoxicity and Antimicrobial Activity of Green Synthesized Silver Nanoparticles Using Nigella sativa Seeds on Wheat Seedlings. J. Chemother. 2022, 9609559.

Fuku, X., Kaviyarasu, K., Matinise, N., Maaza, M., 2016. Punicalagin green functionalized Cu/Cu 2 O/ZnO/CuO nanocomposite for potential electrochemical transducer and catalyst. Nanoscale Res. Lett. 11, 1–12.

Gawlik-Dziki, U., Świeca, M., Sułkowski, M., Dziki, D., Baraniak, B., Czyż, J., 2013. Antioxidant and anticancer activities of Chenopodium quinoa leaves extracts–in vitro study. Food Chem. Toxicol. 57, 154–160.

Harshiny, M., Iswarya, C.N., Matheswaran, M., 2015. Biogenic synthesis of iron nanoparticles using Amaranthus dubius leaf extract as a reducing agent. Powder Technol. 286, 744–749.

Hassan, M., Ismail, M., Moharram, A., Shoreit, A., 2016. Synergistic effect of Biogenic Silver-nanoparticles with β lactam Cefotaxime against Resistant *Staphylococcus arlettae* AUMC b-163 Isolated from T3A Pharmaceutical Cleanroom, Assiut. Egypt. Am. J. Microbiol. Res. 4, 132–137.

Hassan, H., Omoniyi, K., Okibe, F., Nuhu, A., Echioba, E., 2020. Assessment of Wound Healing Activity of Green Synthesized Titanium Oxide Nanoparticles using Strychnos spinosa and Blighia sapida. J. Appl. Sci. Environ. Manag. 24, 197–206.
Hassan, E., Gahlan, A.A., Gouda, G.A., 2023. Biosynthesis approach of copper nanoparticles, physicochemical characterization, cefixime wastewater treatment, and antibacterial activities. BMC Chem. 17, 71.
Hosny, Shimaa, Abd El-Baki, Randa F., Abd El-Wahab, Zeinab H., Gouda, Gamal A., Saddik, Mohammed S., Aljuhani, Ateyatallah, Abu-Dief, Ahmed M., 2023. Development of novel nano-sized Imine complexes using *Coriandrum sativum* extract: structural elucidation, non-isothermal kinetic study, theoretical investigation and pharmaceutical applications. Int. J. Mol. Sci. 24 (8), 14259.
Hosny, S., Shehata, M.R., Aly, S.A., Alsehli, A.H., Salaheldeen, M., Abu-Dief, A.M., Abu-El-Wafa, S.M., 2024. Designing of novel nano-sized coordination compounds based on Spinacia oleracea extract: Synthesis, structural characterization, molecular docking, computational calculations, and biomedical applications. Inorg. Chem. Commun. 160, 111994.
Ijaz, F., Shahid, S., Khan, S.A., Ahmad, W., Zaman, S., 2017. Green synthesis of copper oxide nanoparticles using Abutilon indicum leaf extract: Antimicrobial, antioxidant and photocatalytic dye degradation activitie. Trop. J. Pharm. Res. 16, 743–753.
Imperi, F., Leoni, L., Visca, P., 2014. Antivirulence activity of azithromycin in Pseudomonas aeruginosa. Front. Microbiol. 5, 178.
Jalal, M., Ansari, M.A., Alshamrani, M., Ali, S.G., Jamous, Y.F., Alyahya, S.A., Alhumaidi, M.S., Altammar, K.A., Alsalhi, A., Khan, H.M., 2023. Crinum latifolium mediated biosynthesis of gold nanoparticles and their anticandidal, antibiofilm and antivirulence activity. J. Saudi Chem. Soc. 27, 101644.
Kaur, H., Goyal, V., Singh, J., Kumar, S., Rawat, M., 2019. Biomolecules encapsulated TiO_2 nano-cubes using *Tinospora cordifolia* for photodegradation of a textile dye. Micro & Nano Lett. 14, 1229–1232.
Khalid, A., Ahmad, P., Alharthi, A.I., Muhammad, S., Khandaker, M.U., Faruque, M.R.I., Din, I.U., Alotaibi, M.A., Khan, A., 2021. Synergistic effects of Cu-doped ZnO nanoantibiotic against Gram-positive bacterial strains. PLoS One 16, e0251082.
Kozioł, M.J., 1992. Chemical composition and nutritional evaluation of quinoa (Chenopodium quinoa Willd.). J. Food Compos. Anal. 5, 35–68.
Krishnamoorthi, R., Mahalingam, P.U., Malaikozhundan, B., 2022. Edible mushroom extract engineered Ag NPs as safe antimicrobial and antioxidant agents with no significant cytotoxicity on human dermal fibroblast cells. Inorg. Chem. Commun. 139, 109362.
Madhu, G., Bose, V.C., Maniammal, K., Raj, A.A., Biju, V., 2013. Microstrain in nanostructured nickel oxide studied using isotropic and anisotropic models. Phys. B (Amsterdam, Neth.) 421, 87–91.
Maheswary, T., Nurul, A.A., Fauzi, M.B., 2021. The insights of microbes' roles in wound healing: a comprehensive review. Pharmaceutics 13, 981.
Makarov, V.V., Makarova, S.S., Love, A.J., Sinitsyna, O.V., Dudnik, A.O., Yaminsky, I.V., Taliansky, M.E., Kalinina, N.O., 2014. Biosynthesis of stable iron oxide nanoparticles in aqueous extracts of Hordeum vulgare and Rumex acetosa plants. Langmuir 30, 5982–5988.
Malaikozhundan, B., Vaseeharan, B., Vijayakumar, S., Sudhakaran, R., Gobi, N., Shanthini, G., 2016. Antibacterial and antibiofilm assessment of Momordica charantia fruit extract coated silver nanoparticle. Biocatal. Agric. Biotechnol. 8, 189–196.
Malaikozhundan, B., Vijayakumar, S., Vaseeharan, B., Jenifer, A.A., Chitra, P., Prabhu, N.M., Kannapiran, E., 2017. Two potential uses for silver nanoparticles coated with Solanum nigrum unripe fruit extract: Biofilm inhibition and photodegradation of dye effluent. Microb. Pathog. 111, 316–324.
Malaikozhundan, B., Vinodhini, J., Kalanjiam, M.A.R., Vinotha, V., Palanisamy, S., Vijayakumar, S., Vaseeharan, B., Mariyappan, A., 2020. High synergistic antibacterial, antibiofilm, antidiabetic and antimetabolic activity of Withania somnifera leaf extract-assisted zinc oxide nanoparticle. Bioprocess Biosyst. Eng. 43, 1533–1547.
Malaikozhundan, B., Krishnamoorthi, R., Vinodhini, J., Nambi, K.S.N., Palanisamy, S., 2022a. Multifunctional iron oxide nanoparticles using Carica papaya fruit extract as antibacterial, antioxidant and photocatalytic agent to remove industrial dyes. Inorg. Chem. Commun. 144, 109843.
Malaikozhundan, B., Lakshmi, V.N., Krishnamoorthi, R., 2022b. Copper oxide nanoparticles using Mentha spicata leaves as antibacterial, antibiofilm, free radical scavenging agent and efficient photocatalyst to degrade methylene blue dyes. Mater. Today Commun. 33, 104348.
Mayedwa, N., Mongwaketsi, N., Khamlich, S., Kaviyarasu, K., Matinise, N., Maaza, M., 2018. Green synthesis of nickel oxide, palladium and palladium oxide synthesized via Aspalathus linearis natural extracts: physical properties & mechanism of formation. Appl. Surf. Sci. 446, 266–272.
Miri, A., Khatami, M., Sarani, M., 2020. Biosynthesis, magnetic and cytotoxic studies of hematite nanoparticles. J. Inorg. Organomet. Polym. Mater. 30, 767–774.
Mohamed, W.S., Abu-Dief, A.M., 2018. Synthesis, characterization and photocatalysis enhancement of Eu2O3-ZnO mixed oxide nanoparticles. J. Phys. Chem. Solids 116, 375–385.
Mohammed, H.A., Amin, M.A., Zayed, G., Hassan, Y., El-Mokhtar, M., Saddik, M.S., 2023. In vitro and in vivo synergistic wound healing and anti-methicillin-resistant *Staphylococcus aureus (MRSA)* evaluation of liquorice-decorated silver nanoparticles. J. Antibiot. 76, 291–300.
Navruz-Varli, S., Sanlier, N., 2016. Nutritional and health benefits of quinoa (Chenopodium quinoa Willd.). J. Cereal Sci. 69, 371–376.
Negut, I., Grumezescu, V., Grumezescu, A.M., 2018. Treatment strategies for Infected Wounds. Molecules 23, 2392.
Onyedikachi, O.A., Aisida, S.O., Agbogu, A., Rufus, I., Ahmad, I., Maaza, M., Ezema, F.I., 2022. Zinc ferrite nanoparticles capped with Gongronema latifolium for moderate hyperthermia applications. Appl. Phys. A 128, 95.
Ou, H., Chen, Q., Pan, J., Zhang, Y., Huang, Y., Qi, X., 2015. Selective removal of erythromycin by magnetic imprinted polymers synthesized from chitosan-stabilized Pickering emulsion. J. Hazard. Mater. 289, 28–37.
Panda, K.K., Achary, V.M.M., Krishnaveni, R., Padhi, B.K., Sarangi, S.N., Sahu, S.N., Panda, B.B., 2011. In vitro biosynthesis and genotoxicity bioassay of silver nanoparticles using plants. Toxicol. In Vitro 25, 1097–1105.
Parnham, M.J., Haber, V.E., Giamarellos-Bourboulis, E.J., Perletti, G., Verleden, G.M., Vos, R., 2014. Azithromycin: Mechanisms of action and their relevance for clinical applications. Pharmacol. Ther. 143, 225–245.
Phong, H.X., Viet, N.T., Quyen, N.T.N., Van Thinh, P., Trung, N.M., Ngan, T.T.K., 2022. Phytochemical screening, total phenolic, flavonoid contents, and antioxidant activities of four spices commonly used in Vietnamese traditional medicine. Materials Today: Proceedings 56, A1–A5.
Proksch, E., 2018. pH in nature, humans and skin. J. Dermatol. 45, 1044–1052.
Rajeshkumar, S., Parameswari, R.P., Sandhiya, D., Al-Ghanim, K.A., Nicoletti, M., Govindarajan, M., 2023. Green Synthesis, Characterization and Bioactivity of Mangifera indica Seed-Wrapped Zinc Oxide Nanoparticles. Molecules 28, 2818.
Repo-Carrasco, R., Espinoza, C., Jacobsen, S.-E., 2003. Nutritional value and use of the Andean crops quinoa (Chenopodium quinoa) and kañiwa (Chenopodium pallidicaule). Food Rev. Int. 19, 179–189.
Saddik, M.S., Alsharif, F.M., El-Mokhtar, M.A., Al-Hakkani, M.F., El-Mahdy, M.M., Farghaly, H.S., Abou-Taleb, H.A., 2020a. Biosynthesis, Characterization, and Wound-Healing activity of Phenytoin-Loaded Copper Nanoparticles. AAPS PharmSciTech 21, 175.
Saddik, M.S., Alsharif, F.M., El-Mokhtar, M.A., Al-Hakkani, M.F., El-Mahdy, M.M., Farghaly, H.S., Abou-Taleb, H.A., 2020b. Biosynthesis, characterization, and wound-healing activity of phenytoin-loaded copper nanoparticles. AAPS PharmSciTech 21, 1–12.
Saddik, M.S., Elsayed, M., El-Mokhtar, M.A., Sedky, H., Abdel-Aleem, J.A., Abu-Dief, A. M., Al-Hakkani, M.F., Hussein, H.L., Al-Shelkamy, S.A., Meligy, F.Y., 2022a. Tailoring of Novel Azithromycin-Loaded Zinc Oxide Nanoparticles for Wound Healing. Pharmaceutics 14, 111.
Saddik, M.S., Elsayed, M.M., Abdelkader, M.S.A., El-Mokhtar, M.A., Abdel-Aleem, J.A., Abu-Dief, A.M., Al-Hakkani, M.F., Farghaly, H.S., Abou-Taleb, H.A., 2021. Novel green biosynthesis of 5-fluorouracil chromium nanoparticles using harpullia pendula extract for treatment of colorectal cancer. Pharmaceutics 13 (2), 226.
Saddik, M.S., Elsayed, M.M.A., Abdel-Rheem, A.A., El-Mokhtar, M.A., Mosa, E.S., Al-Hakkani, M.F., Al-Shelkamy, S.A., Khames, A., Daha, M.A., Abdel-Aleem, J.A., 2022b. A Novel C@Fe@Cu Nanocomposite Loaded with Doxorubicin Tailored for the Treatment of Hepatocellular Carcinoma. pharmaceutics, 14, p. 1845.
Salem, H., Samir, E., 2018. Determination of cefotaxime, cefoperazone, ceftazidime and cefadroxil using surface plasmon resonance band of silver nanoparticles. Braz. J. Pharm. Sci. 54.
Sangili, A., Vinothkumar, V., Chen, S.-M., Veerakumar, P., Lin, K.-C., 2021. Efficient and green synthesis of silver nanocomposite using guar gum for voltammetric determination of diphenylamine. J. Mater. Sci. Mater. Electron. 32, 1289–1302.
Santhoshkumar, T., Rahuman, A.A., Jayaseelan, C., Rajakumar, G., Marimuthu, S., Kirthi, A.V., Velayutham, K., Thomas, J., Venkatesan, J., Kim, S.-K., 2014. Green synthesis of titanium dioxide nanoparticles using *Psidium guajava* extract and its antibacterial and antioxidant properties. Asian Pac J Trop Med 7, 968–976.
Senthamarai, M.D., Malaikozhundan, B., 2022. Synergistic action of zinc oxide nanoparticle using the unripe fruit extract of Aegle marmelos (L.) - Antibacterial, antibiofilm, radical scavenging and ecotoxicological effects. Mater. Today Commun. 30, 103228.
Sethy, N.K., Arif, Z., Mishra, P.K., Kumar, P., 2020. Green synthesis of TiO_2 nanoparticles from *Syzygium cumini* extract for photo-catalytic removal of lead (Pb) in explosive industrial wastewater, 9, pp. 171–181.
Shah, M., Fawcett, D., Sharma, S., Tripathy, S.K., Poinern, G.E.J., 2015. Green synthesis of metallic nanoparticles via biological entities. Materials 8, 7278–7308.
Singh, J., Dutta, T., Kim, K.-H., Rawat, M., Samddar, P., Kumar, P., 2018a. Green'synthesis of metals and their oxide nanoparticles: applications for environmental remediation. J. Nanobiotechnol. 16, 1–24.
Singh, J., Mehta, A., Rawat, M., Basu, S., 2018b. Green synthesis of silver nanoparticles using sun dried tulsi leaves and its catalytic application for 4-Nitrophenol reduction. J. Environ. Chem. Eng. 6, 1468–1474.
Singh, J., Kumar, V., Jolly, S.S., Kim, K.-H., Rawat, M., Kukkar, D., Tsang, Y.F.J.J.O.I., Chemistry, E., 2019. Biogenic synthesis of silver nanoparticles and its photocatalytic applications for removal of organic pollutants in water. J. Ind. Eng. Chem. 80, 247–257.
Some, S., Bulut, O., Biswas, K., Kumar, A., Roy, A., Sen, I.K., Mandal, A., Franco, O.L., İnce, İ.A., Neog, K., Das, S., Pradhan, S., Dutta, S., Bhattacharjya, D., Saha, S., Das Mohapatra, P.K., Bhuimali, A., Unni, B.G., Kati, A., Mandal, A.K., Yilmaz, M.D., Ocsoy, I., 2019. Effect of feed supplementation with biosynthesized silver nanoparticles using leaf extract of Morus indica L. V1 on Bombyx mori L. (Lepidoptera: Bombycidae). Sci. Rep. 9, 14839.
Sorg, H., Tilkorn, D.J., Hager, S., Hauser, J., Mirastschijski, U., 2017. Skin wound healing: an update on the current knowledge and concepts. Eur. Surg. Res. 58, 81–94.
Subhapriya, S., Gomathipriya, P., 2018. Green synthesis of titanium dioxide (TiO_2) nanoparticles by *Trigonella foenum-graecum* extract and its antimicrobial properties. Microb. Pathog. 116, 215–220.

Torabian, P., Ghandehari, F., Fatemi, M., 2018. Biosynthesis of iron oxide nanoparticles by cytoplasmic extracts of bacteria lactobacillus casei. Asian J. Green Chem. 2, 181–188.
Vembu, S., Vijayakumar, S., Nilavukkarasi, M., Vidhya, E., Punitha, V.N., 2022. Phytosynthesis of TiO_2 nanoparticles in diverse applications: what is the exact mechanism of action? Sensors Int. 3, 100161.
Vijayakumar, S., Divya, M., Vaseeharan, B., Chen, J., Biruntha, M., Silva, L.P., Durán-Lara, E.F., Shreema, K., Ranjan, S., Dasgupta, N., 2021. Biological compound capping of silver nanoparticle with the seed extracts of Blackcumin (nigella sativa): a potential antibacterial, antidiabetic, anti-inflammatory, and antioxidant. J. Inorg. Organomet. Polym. Mater. 31, 624–635.
Wang, W.-N., Widiyastuti, W., Ogi, T., Lenggoro, I.W., Okuyama, K., 2007. Correlations between crystallite/particle size and photoluminescence properties of submicrometer phosphors. Chem. Mater. 19, 1723–1730.
Wu, G., 2015. Nutritional Properties of Quinoa, pp. 193–210.
Yang, F., Bai, X., Dai, X., Li, Y., 2021. The biological processes during wound healing. Regen. Med. 16, 373–390.
Zachar, O., 2020. Formulations for COVID-19 Early Stage Treatment Via Silver Nanoparticles Inhalation Delivery at Home and Hospital (ScienceOpen Preprints).